ATTENUATION-DIFFERENCE RADAR TOMOGRAPHY: RESULTS OF A MULTIPLE-PLANE EXPERIMENT AT THE U.S. GEOLOGICAL SURVEY FRACTURED-ROCK RESEARCH SITE, MIRROR LAKE, NEW HAMPSHIRE

J.W. Lane, Jr.
United States Geological Survey
11 Sherman Place, U-5015, Storrs Mansfield, CT 06269 USA
jwlane@usgs.gov

F.D. Day-Lewis
Department of Geological and Environmental Sciences, Stanford University
Building 320, Stanford, CA 94305 USA
daylewis@geo.stanford.edu

J.M. Harris
Department of Geophysics, Stanford University
Mitchell Building, Stanford, CA 94305 USA
harris@geo.stanford.edu

F.P. Haeni
United States Geological Survey
11 Sherman Place, U-5015, Storrs Mansfield, CT 06269 USA
phaeni@usgs.gov

S.M. Gorelick
Department of Geological and Environmental Sciences, Stanford University
Building 320, Stanford, CA 94305 USA
gorelick@stanford.edu

ABSTRACT

Attenuation-difference, borehole-radar tomography was used to monitor a series of sodium chloride tracer injection tests conducted within the FSE wellfield at the U.S. Geological Survey Fractured-Rock Hydrology Research Site in Grafton County, New Hampshire, USA. Borehole-radar tomography surveys were conducted by using the sequential-scanning and injection method in three boreholes that form a triangular prism of adjoining tomographic image planes.

Attenuation-difference data were inverted by using a weighted damped least-squares (WDLS) inversion method and several different solution simplicity schemes to suppress tomogram artifacts induced by the acquisition geometry, the location and magnitude of the anomaly, and noisy data. Qualitatively, flat tomograms generated by minimizing the norm of the first spatial derivative were most effective at suppressing artifacts. Although artifact suppression measures can be somewhat effective, negative consequences of artifact suppression include (1) reduction in the magnitude of the attenuation differences in the vicinity of the target anomaly and (2) blurring of the anomalies. These effects distort estimates of the location and magnitude of attenuation anomalies. In order to estimate robustly the location and magnitude of attenuation differences, areal constraints were imposed on the WDLS inversions to confine changes in attenuation to regions that are intersected by rays with large attenuation differences and bounded by rays with insignificant attenuation differences. Results from forward modeling support the application of these constraints. The resolution matrix was used to model the effects of acquisition geometry, target anomaly shape, location, and magnitude. For this study, the method of forward modeling indicates that estimates of pixel attenuation are improved by applying areal constraints to the WDLS inversions.

Analysis of time-lapse attenuation-difference tomograms from the FSE wellfield indicates the network of fractures

that connect the injection well and the pumped wells traverses the tomography-image planes in several different locations.

Assuming the inverted magnitudes of pixel attenuation differences were sufficiently robust, changes in attenuation were interpreted to estimate tracer concentration in the image planes. Secondary-porosity estimates were made by assuming that the tracer concentration in the pixels adjacent to the injection zones was equivalent to the injected concentration. By using this method, the secondary porosity estimates range from 7.5×10^{-4} to 8.5×10^{-4}, which is consistent with estimates reported from previous tracer tests in the FSE wellfield.

The experimental results indicate that attenuation-difference radar tomography can provide high-resolution time-lapse images of the movement of a saline tracer, yielding insight into the three-dimensional spatial distribution of permeable fractures at the site. Planned study efforts will use resolution matrix modeling to optimize acquisition geometry and modified tracer-injection procedures to maximize the resolution of spatial, temporal, and physical property changes that accompany saline-tracer tests.

Key words: Borehole radar, saline tracer, attenuation-difference tomography, fractures, fractured rock, tracer test.

INTRODUCTION

In fractured-rock aquifers, it is difficult to estimate the three-dimensional (3D) geometry and hydraulic properties of fractures and fracture zones. Direct observations of hydraulic properties are limited to the vicinity of boreholes, yet hydraulic conductivity may vary by orders of magnitude over short distances. Geophysical methods can provide valuable information about subsurface structure in regions not sampled by direct means. However, most geophysical methods image contrasts in lithologic properties that may not correlate with contrasts in hydraulic properties in fractured rock. This problem can be overcome by measuring the differences in geophysical measurements taken before, during, and(or) after hydraulic or tracer experiments. The combination of attenuation-difference cross-hole radar tomography and saline-tracer tests has been used to identify the locations of permeable fractures and fracture zones in studies at the U.S. Geological Survey Fractured-Rock Research Site at Mirror Lake, Grafton County, New Hampshire (Wright and others, 1996; Lane, Haeni, and Versteeg, 1998; Wright and Lane, 1998; Lane and others, 1999) and elsewhere (Ramirez and Lytle, 1986; Niva, Olsson, and Blumping, 1988; Olsson, Anderson, and Gustafson, 1991; Olsson and others, 1992; Lane, Joesten and others, 1998). Radar attenuation is a function of electrical conductivity of both the rock and fluid in fractures, whereas attenuation-difference tomography measures changes in fluid conductivity. In effect, the saline tracer illuminates permeable fractures and fracture zones by increasing the fluid salinity in these zones. By imaging time-lapse changes in attenuation, it is possible to estimate the arrival time and concentrations of tracer in the image plane (Lane, Haeni, and Day-Lewis, 1998). This information is valuable for calibration of ground-water flow and transport models.

Lane, Haeni, and Day-Lewis (1998), used a sequential injection and incremental cross-hole scanning (SIIS) method to monitor a slug-injection saline-tracer test. A doublet saline-tracer test was carefully repeated four times under nearly identical conditions. Cross-hole tomography was conducted in a plane approximately parallel to the plane of the injection and extraction wells. During each tracer test, a different portion of the tomographic image plane was scanned at ten-minute intervals. Data collection for a scan occurred over approximately 7 minutes. The cross-hole data from each section collected during identical time intervals were sorted into a series of data sets for tomographic processing and inversion. Tomographic inversions for the FSE2-FSE3 plane were performed using the RAYPT algorithm (Singh and Singh, 1991) in 3DTOM (Jackson and Tweeton, 1996) as previously reported in Lane, Haeni, and Day-Lewis (1998). RAYPT was found to be well-suited to time-lapse attenuation-difference tomography, because attenuation changes were confined to small regions of the image plane. RAYPT was used to constrain changes in attenuation to those tomogram pixels through which highly attenuated rays pass. The results identify kinematic changes in attenuation associated with the transport of the saline tracer through fractures.

In the present study, results for two adjoining tomographic image planes are presented, and inversions using different measures of solution simplicity, including smoothness, flatness, and solution length are compared. We examine model resolution in order to identify artifacts due to source-receiver geometry limitations, and develop additional inversion constraints to better resolve the target anomaly.

FIELD EXPERIMENTS

A series of field experiments using time-lapse cross-hole radar attenuation-difference tomography was conducted in October 1997 and October 1998 at the U.S. Geological Survey Fractured Rock Research Site in the U.S. Forest Service Hubbard Brook Experimental Forest in the Mirror Lake in Grafton County, New Hampshire USA (fig. 1). The purpose of the experiments was to use attenuation-difference tomography to characterize a permeable fracture zone at a depth of about 40 meters (m) in the FSE1-FSE4 well cluster (fig. 2), which consists of four boreholes that approximate a 9-m square.

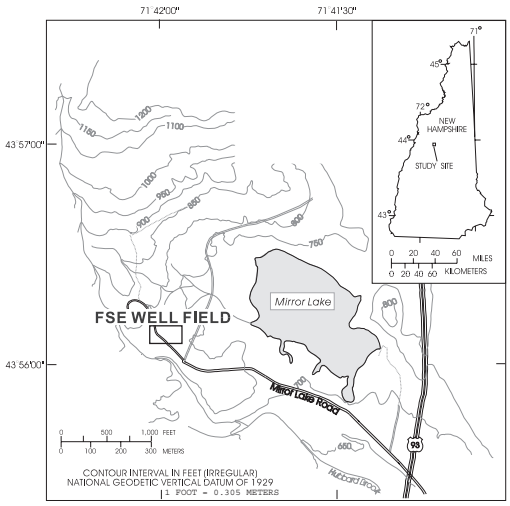

Figure 1. Location of the FSE well field and the US Geological Survey Fractured-Rock Hydrology Research Site near Mirror Lake, Grafton County, New Hampshire, USA.

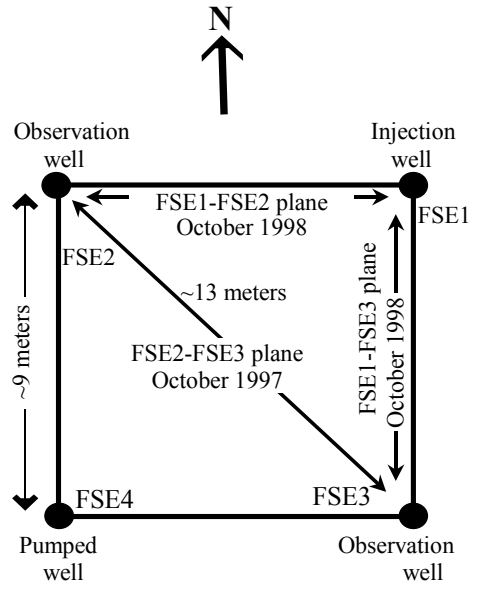

Figure 2. Plan view of the FSE1-FSE4 cluster in the FSE well field at the USGS Fractured-Rock Hydrology Research Site, Grafton County, New Hampshire.

Radar tomography data were collected in three planes during saline tracer tests in the FSE1-FSE4 cluster. Straddle packers were used to isolate the 40-m permeable zone. Specially constructed PVC packers and core pipe were used in the injection and observation boreholes to permit radar logging during the tracer tests (Lane and others, 1998) . Doublet tracer tests were conducted between FSE1 and FSE4 by pumping from the isolated interval in FSE4 at about 4 liter per minute (L/min), while injecting freshwater into the isolated interval in FSE1 at about 2 L/min. After establishing the steady-state flow field, the injection of freshwater was replaced by injection of 20 liters (L) of sodium chloride tracer at a concentration of 50 grams per liter (g/L) into FSE1 over a 10-minute (min) period. After termination of the tracer injection, the freshwater injection was resumed. Samples of the discharge water were collected at 10-min intervals during the first 4 hours (h) of each tracer test, and every 30 min thereafter. The same injection procedures were repeated on consecutive days to collect the necessary cross-hole radar data.

The cross-hole radar-tomography surveys were conducted in three planes—FSE2-FSE3, FSE1-FSE2, and FSE1-FSE3 by using a RAMAC[1] radar system with 100-megahertz (MHz) electric dipole antennas. Data for the FSE2-FSE3 plane were acquired in October 1997; data for the other two planes were acquired in October 1998. For the FSE2-FSE3 plane, ray data were collected in 0.5-m increments from 20 to 70 m below top of casing. For the other two planes, a 0.25-m increment was possible, owing to improvements in acquisition procedures. Radar data were collected continuously every 10 min for 5 h after the start of injection and once again at 8 h after the start of injection.

The data were sorted into equivalent time slices, processed, and analyzed ray-by-ray to identify changes in attenuation with time. Attenuation difference for ray i, d_i, is estimated in decibels (dB) as,

$$d_i = 10 \cdot \log_{10} \left(\frac{\sum_{j=1}^{nsamples} A_{0,j}^2}{\sum_{j=1}^{nsamples} A_j^2} \right) \quad (1)$$

where

$A_{0,j}$ is the amplitude of sample j for trace i in the background data set;

A_j is the amplitude of sample j for trace i in the current time-lapse data set, and

nsamples is the number of samples for the trace.

An example of the amplitude data and computed difference-attenuations for the FSE1-FSE2 20-min data set is shown in figure 3. The effect of the saline tracer on the trace energy is apparent in the amplitude and difference-attenuation data, reducing amplitudes by more than 10 dB for some rays. Certain traces show large increases in attenuation, indicating these rays cross fractures containing the tracer. For the FSE1-FSE2 and FSE1-FSE3 planes, the interwell region that

[1] The use of trade, brand, or firm names in this paper is for identification purposes only and does not constitute an endorsement by the U.S. Geological Survey.

significantly attenuates crossing rays was limited to a small zone in the vicinity of the FSE1 injection interval.

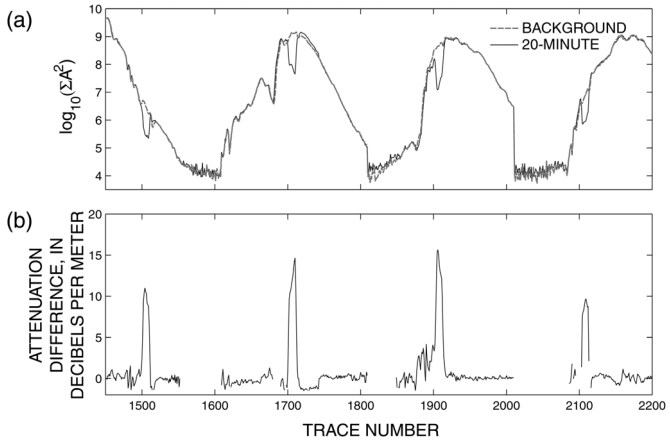

Figure 3. (a) Trace-energy data for the background and 20-minute data sets, and (b) attenuation-difference data.

TOMOGRAPHIC INVERSION

In this study, attenuation-difference data for the FSE1-FSE2 and FSE1-FSE3 planes were inverted using a weighted damped least-squares (WDLS) algorithm and assuming straight rays and various measures of solution simplicity, including smoothness, flatness, and minimum length (Menke, 1989). The WDLS algorithm minimizes (1) the sum of weighted squared differences between the observed and predicted data and (2) some measure of solution complexity (Menke, 1989). The following discussion uses the notation of Menke (1989). For attenuation-difference tomography, the vector of model parameters, **m**, is sought to minimize the function Φ, such that,

$$\Phi(\mathbf{m}) = (\mathbf{d} - \mathbf{Gm})^T \mathbf{W}_e (\mathbf{d} - \mathbf{Gm}) + \varepsilon^2 \mathbf{m}^T \mathbf{D}^T \mathbf{Dm} \quad (2)$$

where,

- **m** is the vector of model parameters, the pixel difference-attenuations;
- $\mathbf{m}^T$ is the matrix transpose of **m**,
- **G** is the data kernel matrix, with elements $\mathbf{G}_{ij}$ equal to the length of ray *i* in pixel *j*;
- $\mathbf{G}^T$ is the matrix transpose of **G**;
- **D** is a variable-weighting matrix chosen to constrain solution simplicity, e.g smoothness;
- $\mathbf{D}^T$ is the matrix transpose of **D**;
- $\mathbf{W}_e$ is a diagonal error-weighting matrix;
- **d** is the vector of measured ray attenuation-differences, and
- ε is the relative weight between prediction error and solution simplicity.

The WDLS estimate, $\mathbf{m}^{est}$, of **m** that minimizes equation 2 is

$$\mathbf{m}^{est} = \left[\mathbf{G}^T \mathbf{W}_e \mathbf{G} + \varepsilon^2 \mathbf{D}^T \mathbf{D}\right]^{-1} \mathbf{G}^T \mathbf{W}_e \mathbf{d}. \quad (3)$$

Due to data limitations, solutions to the tomographic problem are generally non-unique. Without sufficient damping, it may be impossible to compute a WDLS solution (equation 3), or else the resulting tomograms may appear grainy, resembling a checkerboard. Introducing information about solution simplicity may result in unique solutions but can also produce results with undesirable characteristics, such as blurring or anomalies. A number of measures of solution simplicity are possible. **D** is a finite-difference operator, such that the second term of equation 2 corresponds to the norm of the first or second spatial derivative of **m**. Minimization of the norm of the first derivative produces flat tomograms, whereas minimization of the norm of the second derivative produces smooth tomograms. Selecting **D** as an identity matrix results in the damped least-squares or mininum-length solution, which minimizes the sum of squared pixel values. The presence of artifacts due to limited ray data and angular coverage is a common problem in tomographic inversion. If borehole spacing is large relative to borehole length, or if longer path-length, high-angle rays have poor signal-to-noise ratios, tomograms may appear streaky. Features that cannot be resolved can be smeared or spread along ray paths. In some cases, it is difficult to distinguish artifacts from important geophysical anomalies. One way to address this problem is through examination of the model resolution matrix, **R** (Menke, 1989). In order to examine **R**, the matrices **U**, **Λ**, and **V** are determined through singular value decomposition (SVD) of **G**.

$$\mathbf{G} = \mathbf{U}\Lambda\mathbf{V}^T \quad (4)$$

where

- **U** is a matrix of eigenvectors spanning the data space;
- $\mathbf{V}^T$ is the transpose of a matrix of eigenvectors spanning the model space; and
- **Λ** is a diagonal matrix containing the singular values of G.

The resolution matrix, **R**, is defined by,

$$\mathbf{R} = \mathbf{V}_p \mathbf{V}_p^T \quad (5)$$

where

- **R** is the model resolution matrix, a symmetric matrix with rows (or columns) describing the local averaging of parameter estimates, and
- $\mathbf{V}_p$ is the columns of V corresponding to the p non-zero singular values.

Computed in this manner, **R** corresponds to the model resolution expected for a damped least-squares inversion, and can be examined to estimate pixel resolution in different

regions of tomograms. In addition, **R** provides a way to directly examine the effects of a given source-receiver geometry on inversions. For a given acquisition geometry, **R** is used to predict what an inversion would yield, $\mathbf{m}^{pred}$, for a hypothetical difference-attenuation model $\mathbf{m}^{true}$,

$$\mathbf{m}^{pred} = \mathbf{R}\mathbf{m}^{true} \tag{6}$$

where

$\mathbf{m}^{pred}$ is the predicted result of an inversion for error-free data calculated for $\mathbf{m}^{true}$, and

$\mathbf{m}^{true}$ is the true attenuation difference.

By use of equation 6, forward modeling (using **R** based on the data acquisition geometry used in this study) provided a means to identify probable inversion artifacts and to guide the development of a conceptual model that describes the shape and location of our target anomaly, which is consistent with plots of rays that do not show significant differences in attenuation (fig. 7). The constrained WDLS inversion of the field data assumes pixel attenuations do not change outside the inferred region of the target anomaly. Linear equality constraints on pixel difference-attenuations could be imposed by using either quadratic constraints or Lagrange multipliers. For this problem, where the values are constrained to zero outside the region of the anomaly and unconstrained within, the equality constraints were implemented by modifying our forward model, **d**=**Gm**, to be

$$\mathbf{d'} = \mathbf{G'}\mathbf{m'} \tag{7}$$

where

G' is a matrix containing the columns of the ray path matrix corresponding to the unconstrained pixels inside the assumed region of the target anomaly;

m' is a vector of the difference-attenuation in the unconstrained pixels, and

d' is a vector containing the data for rays crossing the target anomaly.

Whereas unconstrained, smooth, or flat tomograms tend to underestimate the attenuation within the target region, the constrained inversion should yield values that are more appropriate for computing tracer concentration from attenuation differences.

In this study, an effective media approach is used to interpret differences in attenuation given by,

$$\alpha = \omega\sqrt{\mu\varepsilon}\left\{\frac{1}{2}\left[\sqrt{\left(\frac{\sigma}{\omega\varepsilon}\right)^2 + 1} - 1\right]\right\}^{\frac{1}{2}} \tag{8}$$

where

α is the radar attenuation in Nepers per meter (Np/m);

ω is frequency in radians;

μ is the magnetic susceptibility in Henries per meter (H/m);

ε is the dielectric permittivity in Farads per meters (F/m); and

σ is the electrical conductivity in Siemens per meter (S/m).

Differences in attenuation are induced by changes in conductivity, Δσ, and the secondary (fracture) porosity, ϕ_S, where fluid specific conductance is given by

$$\boldsymbol{\sigma}_{\mathbf{f}} \approx \frac{\Delta\sigma}{\phi_S} * 10^4 \tag{9}$$

where

$\boldsymbol{\sigma}_{\mathbf{f}}$ is fluid specific conductance, in μS/cm, and

ϕ_S is an estimate of secondary porosity.

By using data from Draknov (1962), that is tabulating the specific conductance of sodium chloride solutions for a range of temperatures, an estimate of sodium chloride concentration at a temperature of 20^0 C can be calculated from specific conductance by

$$\boldsymbol{C} \approx 7\text{x}10^{-1}\,\sigma_f \tag{10}$$

where

C is the sodium chloride concentration, in mg/L.

RESULTS

In a previous study, Lane, Haeni, and Day-Lewis (1998) reported attenuation-difference tomography results for the FSE2-FSE3 plane. The results indicated that the relative tracer concentrations in the vicinity of FSE2 were higher than in the vicinity of FSE3 and that the peak radar attenuation (or saline tracer concentration) occurred in the FSE2-FSE3 plane about 2 h after injection. In this study, some of the effects of data acquisition geometry and inversion constraints on tomograms are examined to provide further insight into the transport of saline tracers in fractured-rock aquifers.

Measures of Solution Simplicity

Tomograms were generated using several different criteria for solution simplicity, including minimum length, flatness, and smoothness (figs. 4a, 4b, and 4c). Differences between the tomograms show the effects of the different solution simplicity weighting matrices; similarities are due to the data and to acquisition geometry artifacts. The tomogram artifacts demonstrate the trade-off in the experiment between spatial and temporal resolution. To image time-lapse changes in tracer concentration, tomographic scans were

collected every ten minutes, a time constraint severely limiting the number of rays collected per scan.

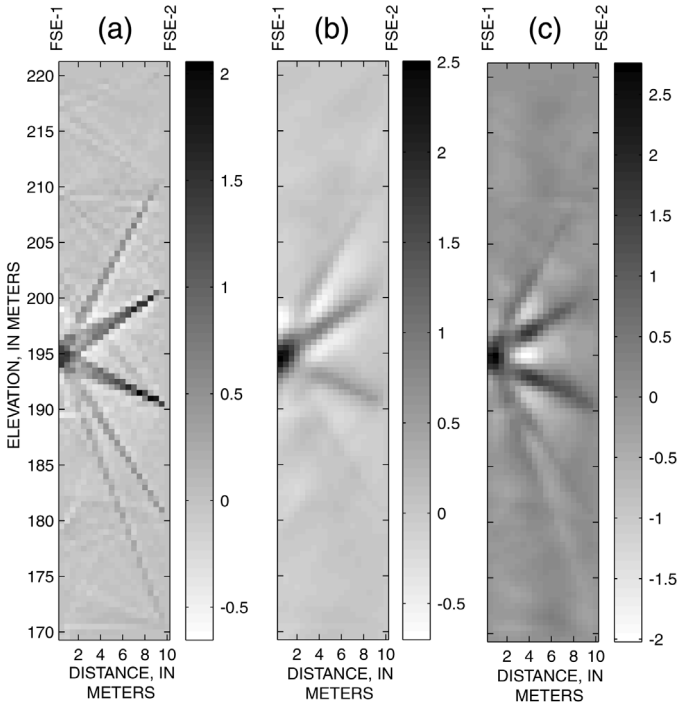

Figure 4. Tomograms generated using (a) solution length, (b) flatness, and (c) smoothness as measures of solution simplicity. Attenuation difference (right-hand scale) is in decibels per meter.

The streaky appearance of the tomograms shown in figure 4 is an artifact of the data acquisition geometry. By increasing the weight assigned to the measure of solution simplicity, the artifacts can be suppressed. The consequences of artifact suppression include (1) reduction in the magnitude of the attenuation differences in the vicinity of the target anomaly and (2) blurring of the anomalies. These effects may be unimportant if the object of a study is to qualitatively image structure and not to estimate true attenuation difference. However, to robustly estimate tracer concentrations from attenuation values, it is important to have accurate estimates. Blurring of the anomalies can over-estimate the dimensions of the region of tracer migration. Comparing flat, smooth, and damped inversion methods, the flat inversions are qualitatively superior. Smooth inversions are prone to oscillations, which include spurious negative anomalies. The damped inversions are severely affected by data acquisition artifacts.

Model Resolution

The elements of the diagonal of **R**, the model resolution matrix, are displayed as a tomogram in figure 5a. Pixels with greater values are better resolved, whereas pixels with lower values are less resolved. A pixel with a value of 1 would be perfectly resolved; that is, there are sufficient data to yield a unique estimate for the attenuation difference in that pixel. The column of **R** corresponding to a pixel in the vicinity of the apparent anomaly near FSE1 is shown in figure 5b. This figure indicates that estimates of attenuation difference for this pixel are averaged with the values of other pixels along paths of greater ray density. To further investigate the apparent artifacts, the resolution matrix was used to predict an inverted result for a simple, hypothetical model. For a hypothetical model with an attenuation difference of 6 dB/m in a block of pixels near the tracer-injection interval (fig. 5c), the predicted inverted result (fig. 5d) contains streaks very similar to those in the inversions of the difference data (fig. 4). Furthermore, the inverted attenuation-difference values are considerably lower than the true values within the target anomaly. The results of the forward modeling indicate (1) that the streaks present in the tomograms shown in figure 4 are artifacts, and (2) the true attenuation near the injection zone is probably higher than indicated by the inversions. These results lead to the development of an additional areal constraint that is based on plots of rays that do not exhibit significant differences in attenuation (fig. 6). Changes in attenuation were constrained to the area bounded by these rays; this limited changes in attenuation to a cluster of pixels in the vicinity of the injection interval. Attenuation-difference tomograms resulting from areally constrained WDLS inversions for the FSE1-FSE2 and FSE1-FSE3 planes are shown in figure 7.

Tracer Transport Behavior and Sodium Chloride Concentration in the FSE1-FSE2 and FSE1-FSE3 Planes

The time-lapse series of tomograms shown in figure 7 indicated that the tracer leaves the FSE1-FSE2 and FSE1-FSE3 image planes after traveling only a few meters from the injection point in FSE1. Based on the tomographic results for all three planes, it appears that the network of fractures connecting FSE1 (injection well) and FSE4 (pumped well) (fig. 2) moves the tracer out of the FSE1-FSE2 and FSE1-FSE3 image planes, through pathways close to FSE2. The tracer identified in the FSE2-FSE3 plane (Lane, Haeni, and Day-Lewis, 1998) is not observed in the FSE1-FSE2 tomograms, which may indicate the fractures are not directly connected with FSE2, or are not illuminated due to limitations in the acquisition geometry or other effects, such a fracture orientation bias.

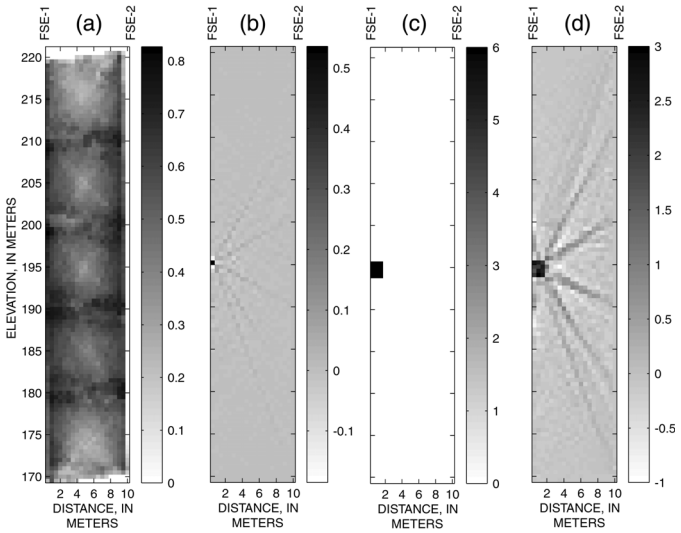

Figure 5. (a) Elements of the diagonal of the model resolution matrix (dimensionless) displayed in the corresponding tomogram pixels; (b) the model resolution (dimensionless) for a single pixel in the vicinity of the injection interval; (c) a hypothetical model of pixel difference-attenuations, and (d) the predicted tomographic inversion for the synthetic model of (c). Attenuation difference (right-hand scale) is in decibels per meter.

An example of the estimate of tracer concentration (equations 8 to 10) is shown in figure 8 for the 20-min time-step tomograms for both the FSE1-FSE2 and FSE1-FSE3 planes. The tomograms were calibrated by solving for secondary porosity using equations 9 and 10, assuming the early-time maximum attenuation near the injection point was induced by tracer with the initial concentration of 5×10^4 mg/L. Using this method, we estimate secondary porosity is about 7.5×10^{-4} in the FSE1-FSE2 plane and about 8.5×10^{-4} in the FSE1-FSE3 plane. Both estimates are lower than the secondary porosity of 1×10^{-3} reported by Shapiro (1996) for the FSE wellfield, which is based on hydraulic and tracer tests. Because it is likely that some dilution of the tracer occurs during injection, the secondary porosity estimated by this method is considered as a lower bound.

Estimates of the maximum tracer concentration in the FSE1-FSE2 and FSE1-FSE3 image planes using the maximum attenuation difference for each time-step is shown in figure 9. The rapid decrease in attenuation differences with time is interpreted as movement of the saline tracer out of the image planes.

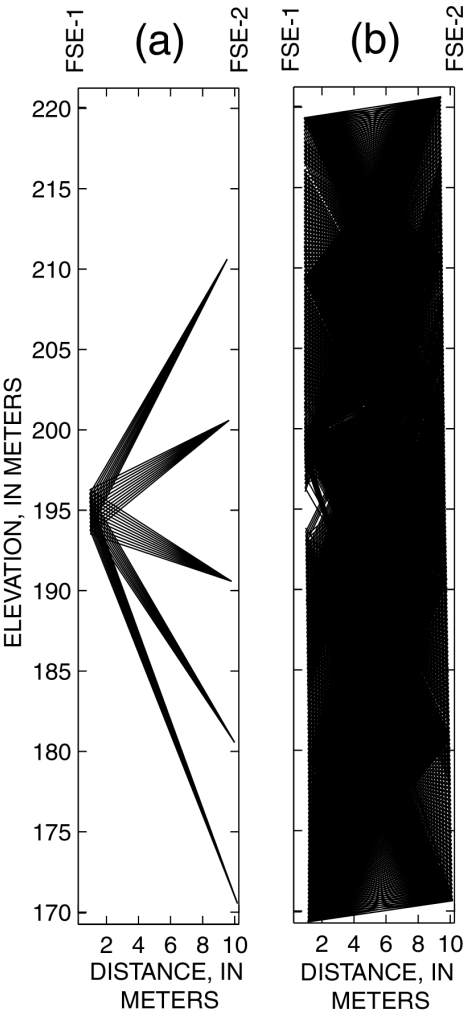

Figure 6. Plots of (a) rays with an attenuation difference greater than the mean attenuation difference plus two standard deviations (high-attenuation rays) and (b) rays with an attenuation difference less than the mean attenuation difference plus one standard deviation (low attenuation rays).

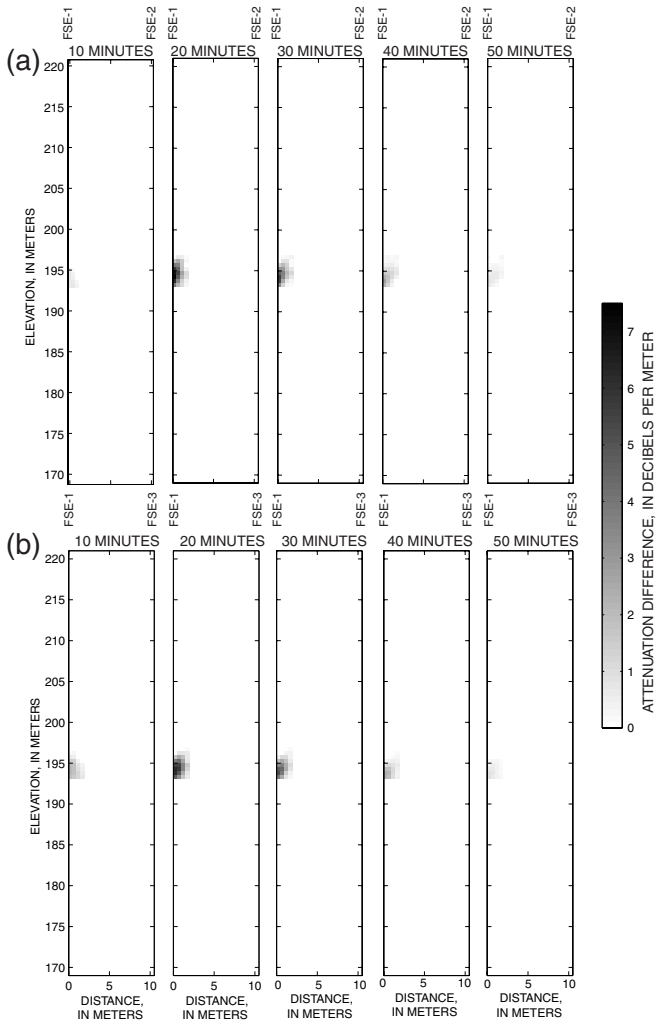

Figure 7. Time-lapse attenuation-difference tomography sequence for (a) the FSE1-FSE2 plane and (b) the FSE1-FSE3 plane using areally constrained weighted damped least-squares inversion.

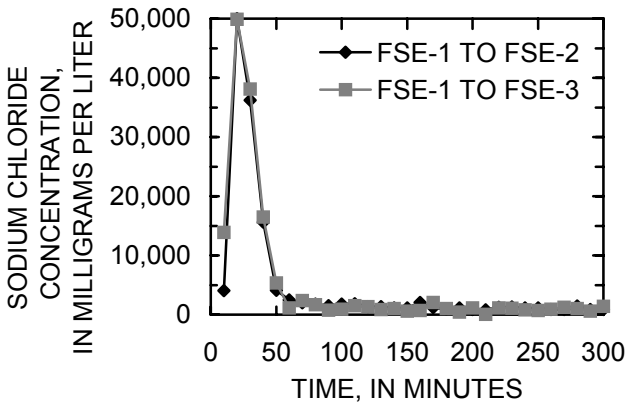

Figure 8. Estimate of maximum sodium chloride concentration for the FSE1-FSE2 and FSE1-FSE3 planes plotted against time. Concentrations were calculated for each time-step using the maximum pixel attenuation difference in each tomogram.

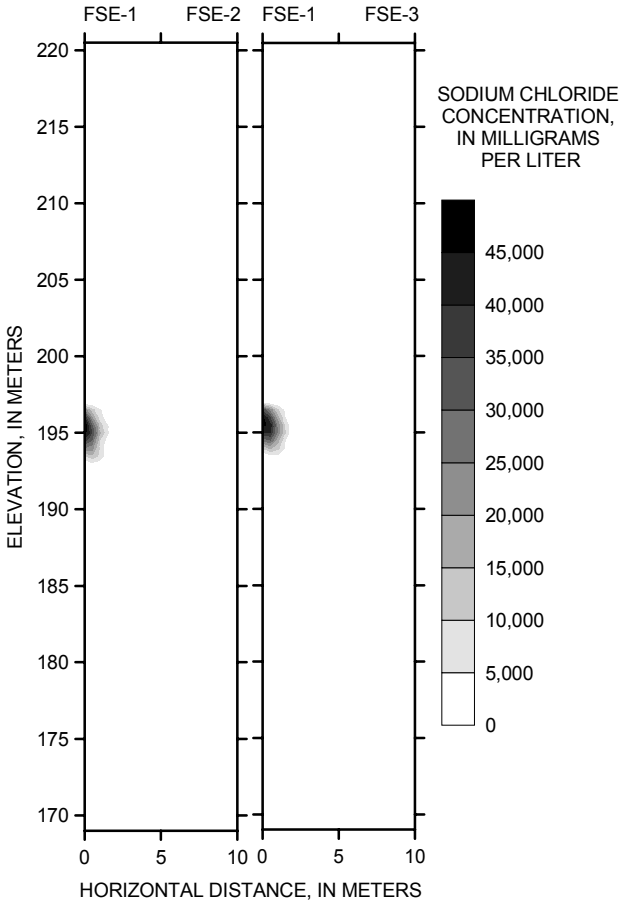

Figure 9. Estimates of sodium chloride concentration (milligrams per liter) in the FSE1-FSE2 plane (left) and FSE1-FSE3 plane (right), 20 minutes after the injection of tracer.

CONCLUSIONS

Results of attenuation-difference radar tomography used to monitor a series of saline tracer injection tests conducted within the FSE wellfield at the U.S. Geological Survey Fractured-Rock Research Site, Grafton County, New Hampshire, USA, indicate that time-lapse tomography methods can provide high-resolution images of tracer distribution in permeable zones. The distribution of tracer in the tomograms can provide important insights into the geometry and hydraulic properties of fractured-rock aquifers.

Design of the data acquisition geometry is a critical component of time-lapse tomography, requiring a trade-off between spatial and temporal resolution. Artifacts in tomograms that result from the data acquisition geometry can be misinterpreted, and need to be suppressed. In this study, a WDLS inversion method was used with different solution simplicity measures to suppress artifacts. Minimization of the norm first spatial derivative to produce flat tomograms proved qualitatively superior to smooth WDLS and damped least-squares inversions. Use of artifact suppression has negative consequences that include (1) reduction in the magnitude of the difference-attenuations in the vicinity of the target anomaly and (2) blurring of the anomalies.

For studies that seek to image structure, these effects may be unimportant. However, if robust estimates of the location and physical properties of the target anomaly are of interest, a different approach to artifact suppression is needed. In this study the application of the resolution matrix and the use of areal inversion constraints that are based on the attenuation difference behavior of rays intersecting and bounding attenuation zones were examined. The resolution matrix can be used to forward model the effects of acquisition geometry and target anomaly shape, properties, and location within the image plane. Through forward modeling, data acquisition artifacts can be predicted to aid (1) interpretation of field data and (2) design of the acquisition geometry. Examination of ray attenuation differences can provide information useful for designing areal inversion constraints. If rays that show small attenuation differences bound zones with high attenuation difference, then constraining the inversions to permit attenuation to change in the bounded areas may be justified. The use of this type of constraint minimizes acquisition geometry artifacts and can decrease the error of the estimated parameter.

If estimates of pixel attenuation differences are sufficiently robust, changes in attenuation can be interpreted in terms of fluid conductivity and tracer concentration, provided secondary porosity is available or can be estimated. For this study, estimates of secondary porosity were made by assuming that the tracer concentration in the pixels adjacent to the injection zones was known.

Application of the areally constrained WDLS inversion method to attenuation-difference radar-tomography data from the FSE1-FSE2 and FSE1-FSE3 planes produced tomograms that minimized artifacts and maximized pixel resolution. The time-lapse tomograms indicate the tracer leaves the FSE1-FSE2 and FSE1-FSE3 image planes within 50 min after injection of the tracer and travels only a few meters in the image planes from the injection point in FSE1. The experimental results provide important insights into the nature of transport in the fractured rock aquifer in the FSE wellfield. Based on the tomographic results for all three planes, it appears that the network of fractures connecting FSE1 and FSE4 has a complex geometry that either does not cross much of the image planes, or connects in ways that are not robustly imaged by the tomographic methods used to date. Planned study efforts will use resolution matrix modeling to optimize acquisition geometry and modify tracer-injection procedures to maximize spatial, temporal, and physical-property resolution.

ACKNOWLEDGEMENTS

This study was supported by the U.S. Geological Survey Toxic Substances Hydrology program. Fred Day-Lewis and Steven Gorelick gratefully acknowledge National Scioence Foundation support through grants numbered EAR-9705812 and EAR-9707031, and Jerry Harris acknowledges support from U. S. Environmental Protection Agency STAR Fellowship U-915155-01-0. The USGS Fractured-Rock Research Site is located within the Hubbard Brook Experimental Forest, operated by the Northeastern Forest Experiment Station, U.S. Department of Agriculture Forest Service, Radnor, Pennsylvania.

REFERENCES

Dakhnov, V.N., 1962. *Interpretatsiya rezultatov geofizicheskikh issledovanii razrezov skvazhin*, ed. 2, Moscow, Gosudar. Nauch.-Tekh. Izd. Neft. I Gorno-Topliv. Lit., 547 pp.

Jackson, M.J. and D.R. Tweeton, 1996. 3DTOM: three-dimensional geophysical tomography. *U.S. Bureau of Mines Report 9617,* 84 pp.

Lane, J.W., Jr., Haeni, F.P., Day-Lewis, F.D., 1998. Use of time-lapse attenuation-difference radar tomography methods to monitor saline tracer transport in fractured crystalline bedrock, GPR'98, Seventh International Conference on Ground Penetrating Radar, Lawrence, KS, May 27-30, pp. 533-538.

Lane, J.W., Jr., Haeni, F.P., Versteeg, R., 1998. Use of a multi-offset borehole-radar reflection method in fractured crystalline bedrock at Mirror Lake, Grafton County, New Hampshire, *Proceedings of the Symposium on the Application of Geophysics to Engineering and Environmental Problems*, March 22-26, Chicago, Ill., 1998, pp. 359-368.

Lane, J.W., Jr., Joesten, P.K., Haeni, F.P., Vendl, M., Yeskis, D., 1998. Use of borehole-radar methods to monitor the movement of a saline tracer in carbonate rock at Belvidere, Illinois. *Proceedings of the Symposium on the Application of Geophysics to Engineering and Environmental Problems*, March 22-26, Chicago, Ill., pp. 323-332.

Lane, J.W., Jr., Wright, D.L., and Haeni, F. P., 1999. Borehole radar tomography using saline tracer injections to image fluid flow in fractured rock. *Proceedings of the U.S. Geological Survey Toxic Substances Hydrology Program, U.S. Geological Survey Water-Resources Investigation Report 99-4018C*, v. 3, pp. 747-756.

Niva, B., O. Olsson, and P. Blumping, 1988. Radar crosshole tomography at the Grimsel Rock Laboratory with application to migration of saline tracer through fracture zones, *Nationale Genossenschaft fur die lagerung radioaktiver Abfalle, NTB 88-31*, 87 pp.

Menke, W., 1989. *Geophysical Data Analysis: Discrete Inverse Theory, Revised Edition*: San Diego, Academic Press Inc., 289 pp.

Olsson, O., P. Anderson, S. Carlsten, L. Falk, B. Niva, and E. Sandberg, 1992. Fracture characterization in crystalline rock by borehole radar, *Ground penetrating radar*, J. Pilon (ed.), Geological Survey of Canada Paper 90-4, pp. 139-150.

Olsson, O., P. Anderson, and E. Gustafson, 1991. Site characterization and validation-monitoring saline tracer transport by borehole radar measurements, Final report, Stripa Project, TR 91-18, Swedish Nuclear Fuel and Waste Management Company, Stockholm, Sweden, 155 pp.

Ramirez, A.L. and R.J. Lytle,1986. Investigation of fracture flow paths using alterant geophysical tomography, *Journal of Rock Mechanics and Mining Sciences and Geomechanics*, vol.23, no.2, pp. 165-169.

Singh, R.P. and Y.P. Singh, 1991. RAYPT: A new technique for inversion of geotomographic data, *Geophysics*, vol. 56, no. 8, pp. 1215-1227.

Shapiro, A.M., 1996. Estimation of effective porosity in fractured crystalline rock by controlled tracer tests, in Stevens, P.R., and Nicholson, T.J., eds., Joint U.S. Geological Survey, U.S. Nuclear Regulatory Commission Workshop on research related to low-level radioactive waste disposal, May 4-6, 1993, National Center, Reston, VA: U.S. Geological Survey Water-Resources Investigations Report 95-4015, pp. 185-190.

Wright, D.L., T.P. Grover, K.J. Ellefsen, J.W. Lane Jr., and P.G. Kase, 1996. Radar Tomograms at Mirror Lake, New Hampshire: 3-D Visualization and a Brine Tracer Experiment, *Proceedings of the Symposium on the Application of Geophysics to Engineering and Environmental Problems*, April 28 - May 2, 1996, Keystone, CO, pp. 565-575.

Wright, D.L., and J.W. Lane Jr., 1998. Mapping hydraulically permeable fractures using directional borehole radar and hole-to-hole tomography with a saline tracer, *Proceedings of the Symposium on the Application of Geophysics to Engineering and Environmental Problems*, March 22-26, 1998, Chicago, Ill., pp. 379-388.